



# A comparative study of lithium-storage performances of hematite: Nanotubes vs. nanorods



Liang Chen<sup>a</sup>, Huayun Xu<sup>a</sup>, Li'e Li<sup>a</sup>, Fangfang Wu<sup>a</sup>, Jian Yang<sup>a,\*</sup>, Yitai Qian<sup>a,b</sup>

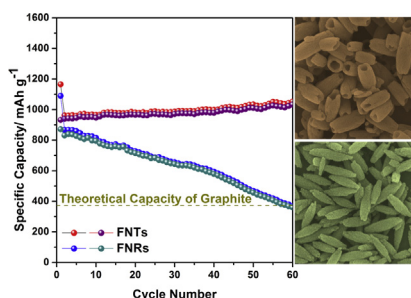
<sup>a</sup>Key Laboratory of Colloid and Interface Chemistry, Ministry of Education, and School of Chemistry and Chemical Engineering, Shandong University, Jinan 250100, PR China

<sup>b</sup>Hefei National Laboratory for Physical Science at Microscale, and Department of Chemistry, University of Science and Technology of China, Hefei 230026, PR China

## HIGHLIGHTS

- $\alpha$ -Fe<sub>2</sub>O<sub>3</sub> nanotubes and nanorods with close sizes are obtained by hydrothermal methods.
- The nanotubes show better cycling stability and rate capability than the nanorods.
- The nanotubes show a high capacity of 810 mAh g<sup>-1</sup> at 1 A g<sup>-1</sup> after 60 cycles.

## GRAPHICAL ABSTRACT



## ARTICLE INFO

### Article history:

Received 22 March 2013

Received in revised form

4 June 2013

Accepted 21 June 2013

Available online 5 July 2013

### Keywords:

Hematite

Nanotubes

Nanorods

Lithium-ion battery

## ABSTRACT

$\alpha$ -Fe<sub>2</sub>O<sub>3</sub> nanotubes and nanorods are obtained via a hydrothermal method without further annealing. Both of them are characterized by X-ray powder diffraction, scanning electron microscopy, and high-resolution transmission electron microscopy. The lithium-storage performances of the nanostructures are measured and compared in terms of reversible capacity, cycling stability, and rate capability. The electrode based on the nanotubes delivers the reversible capacities of 1200 mAh g<sup>-1</sup> at 100 mA g<sup>-1</sup>, 1000 mAh g<sup>-1</sup> at 500 mA g<sup>-1</sup>, and 810 mAh g<sup>-1</sup> at 1000 mA g<sup>-1</sup> after 60 cycles, much higher than those based on the nanorods. The better performances of the nanotubes could be assigned to their tubular morphology that tolerates the huge volume change during the discharge/charge processes and possesses the large surface area to increase the contact between the electrode and the electrolyte. These insights will be of benefits in the design of other anode materials for lithium ion batteries.

© 2013 Elsevier B.V. All rights reserved.

## 1. Introduction

Lithium-ion batteries (LIBs) as a clean and reliable energy storage device, have been widely applied in many fields, such as portable electronics, pure electric or hybrid electric vehicles, smart power grids and so on. These applications not only greatly

stimulate the development of LIBs, but also propose a high expectation on electrodes with high energy density and strong power density. Recently, transition metal oxides have attracted much attention owing to their markedly high specific capacity as the anode materials of LIBs [1]. Among numerous transition metal oxides, hematite ( $\alpha$ -Fe<sub>2</sub>O<sub>3</sub>) stands out from others, due to its low toxicity, high abundance, and most importantly, high theoretical specific capacity (1007 mAh g<sup>-1</sup>). However, hematite suffers over a large volume variation of approximate 96% during discharge/charge cycles [2], much higher than the commercially available

\* Corresponding author. Tel./fax: +86 531 88364489.

E-mail address: [yangjian@sdu.edu.cn](mailto:yangjian@sdu.edu.cn) (J. Yang).

anode, graphite, that only experiences a volume change of 10% [3]. The huge volume change would result in the pulverization of the anode and the loss of electrical connectivity. Thus, the reversible capacity of hematite usually quickly decays upon cycling, which greatly hinders its application in LIBs.

In order to address this issue, many efforts have been devoted to the control on the size, shape and structure of the electrode materials [4]. A myriad of hematite nanostructures have been synthesized for LIBs, such as nanoparticles [5–7], nano-sheets [8,9], nanoflakes [10–13], nanoflowers [14–16], nanotubes [17–19] and nanorods [20–24]. Among these nanostructures, one-dimensional (1D) morphology has been demonstrated to be very appealing, due to its superior charge-transfer kinetics to the 3D counterparts [25,26]. Hematite nanorods as an anode for LIBs were first reported by Xie's group in 2006 [20]. They found that the initial discharge/charge performances are highly related with the size and surface area of the nanorods. But the long-term cycling performance was not shown. Later, this data has been provided by Mullin's group. The single-crystalline  $\alpha$ -Fe<sub>2</sub>O<sub>3</sub> nanorods retained a reversible capacity of 837 mAh g<sup>-1</sup> at a current density of 503 mA g<sup>-1</sup> after 100 cycles [23]. Compared with nanorods, nanotubes have a hollow space inside, which is supposed to effectively alleviate the capacity fading caused by the large volume variation and give an improved lithium-storage performance. In spite of this, the direct and comprehensive comparison between the nanorods and the nanotubes of  $\alpha$ -Fe<sub>2</sub>O<sub>3</sub> has not been conducted to the best of our knowledge, although hematite nanotubes for LIBs have been examined in literature [17–19].

Herein, the single-crystalline  $\alpha$ -Fe<sub>2</sub>O<sub>3</sub> nanorods and nanotubes are synthesized via a hydrothermal method without further annealing. Both of them show the close sizes and size distributions. But the nanotubes exhibit the better lithium-storage performances in terms of reversible capacity, capacity retention and rate performance than the nanorods. The underlying reasons for the superior performances of the nanotubes are discussed based on *ex situ* transmission electron microscopy, current interruption technique and electrochemical impedance spectra.

## 2. Experimental section

### 2.1. Synthesis method

The syntheses for the hematite nanotubes/nanorods were slightly modified based on a previous report [27]. In a typical procedure for hematite nanotubes, FeCl<sub>3</sub> (0.6488 g), NH<sub>4</sub>H<sub>2</sub>PO<sub>4</sub> (0.0166 g) and Na<sub>2</sub>SO<sub>4</sub> (0.0156 g) were dissolved in 200 mL deionized water. The solution was transferred into a Teflon-lined autoclave and kept at 220 °C for 48 h. After that, the precipitates were collected by centrifugation, washed with distilled water and absolute ethanol, and dried in air at 80 °C. The obtained  $\alpha$ -Fe<sub>2</sub>O<sub>3</sub> nanotubes were labeled as FNTs. The  $\alpha$ -Fe<sub>2</sub>O<sub>3</sub> nanorods, denoted as FNRs, were prepared by the similar recipe without Na<sub>2</sub>SO<sub>4</sub>. Meanwhile, the reaction temperature and time were adjusted to 180 °C and 24 h, respectively.

### 2.2. Characterization

The X-ray powder diffraction (XRD) patterns of the products were characterized by Bruker D8 advanced X-ray diffractometer with Cu K $\alpha$  radiation ( $\lambda = 1.5418$  Å). The structure and morphology of the samples were observed by a field emission scanning electron microscope (SEM, JEOL-JSM-6700F), a transmission electron microscope (TEM, JEM-1011) with an accelerating voltage of 100 kV, and a high resolution transmission electron microscope (HRTEM, JEOL-2010) operating at 200 kV. N<sub>2</sub> adsorption–desorption

isotherms were measured on a Micromeritics ASAP-2000 analyzer. The specific surface areas were calculated by the Brunauer–Emmett–Teller (BET) method.

### 2.3. Electrochemical measurements

The electrochemical tests were carried out within CR2032 coin cells. The  $\alpha$ -Fe<sub>2</sub>O<sub>3</sub> electrode film was composed of 60 wt% FNTs (or FNRs) as the active material, 20 wt% acetylene black as the conductive additive, and 20 wt% sodium carboxymethyl cellulose binder (CMC) as a binder. Then, it was assembled in an argon-filled glove box (Mikrouna, Super 1220/750/900) with a lithium foil as the counter and reference electrode, a mixture of 1 M LiPF<sub>6</sub> in ethylene carbonate (EC)–ethyl methyl carbonate (EMC)–dimethyl carbonate (DMC) (1:1:1 by volume) as the electrolyte, and a Celgard 2300 microporous membrane as the separator. Galvanostatic discharge–charge cycles of cells were performed at room temperature using Land CT2001A battery cycler (Xinnuo, Wuhan China) in the voltage range of 0.05–3.0 V (vs. Li<sup>+</sup>/Li) at different current densities. Electrochemical impedance spectroscopy (EIS) was measured on an FRA-520 (MaterialsMates, Italia) connected to a Potentiostat-510 (MaterialsMates) over the frequency range of 100 kHz–0.01 Hz. DC resistance was measured at a pulse of 18 s at every 5% increase of SOC (state of charge). Then, the DC resistance ( $R_{dc}$ ) could be obtained by  $R_{dc} = \Delta U/I$ , where  $\Delta U$  is the voltage variation before and after the interruption [28].

## 3. Result and discussion

### 3.1. Structure and morphology characterizations

Fig. 1 shows the X-ray powder diffraction (XRD) patterns of the nanotubes (FNTs) and the nanorods (FNRs). All of the reflection peaks can be indexed as  $\alpha$ -Fe<sub>2</sub>O<sub>3</sub> (space group *R*-3c, JCPDS No. 33-0664), confirming that both of the FNTs and FNRs are in a corundum structure without impurities.

Fig. 2 shows the SEM, TEM, HRTEM images, and SAED patterns of the FNTs and the FNRs. As shown in Fig. 2a and b, the length, inner diameter and outer diameter of the FNTs are in the ranges of 150–350 nm, 50–80 nm and 90–100 nm, respectively. The HRTEM image (Fig. 2c, d) and the SAED pattern (the inset of Fig. 2d) confirm that the nanotubes can be identified as  $\alpha$ -Fe<sub>2</sub>O<sub>3</sub>, consistent with the

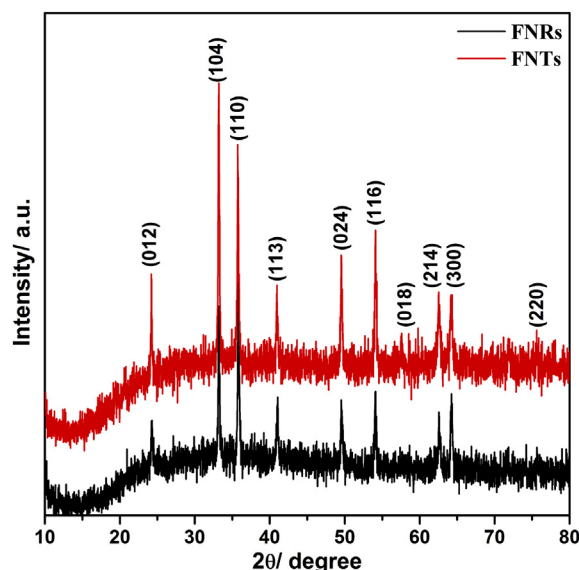
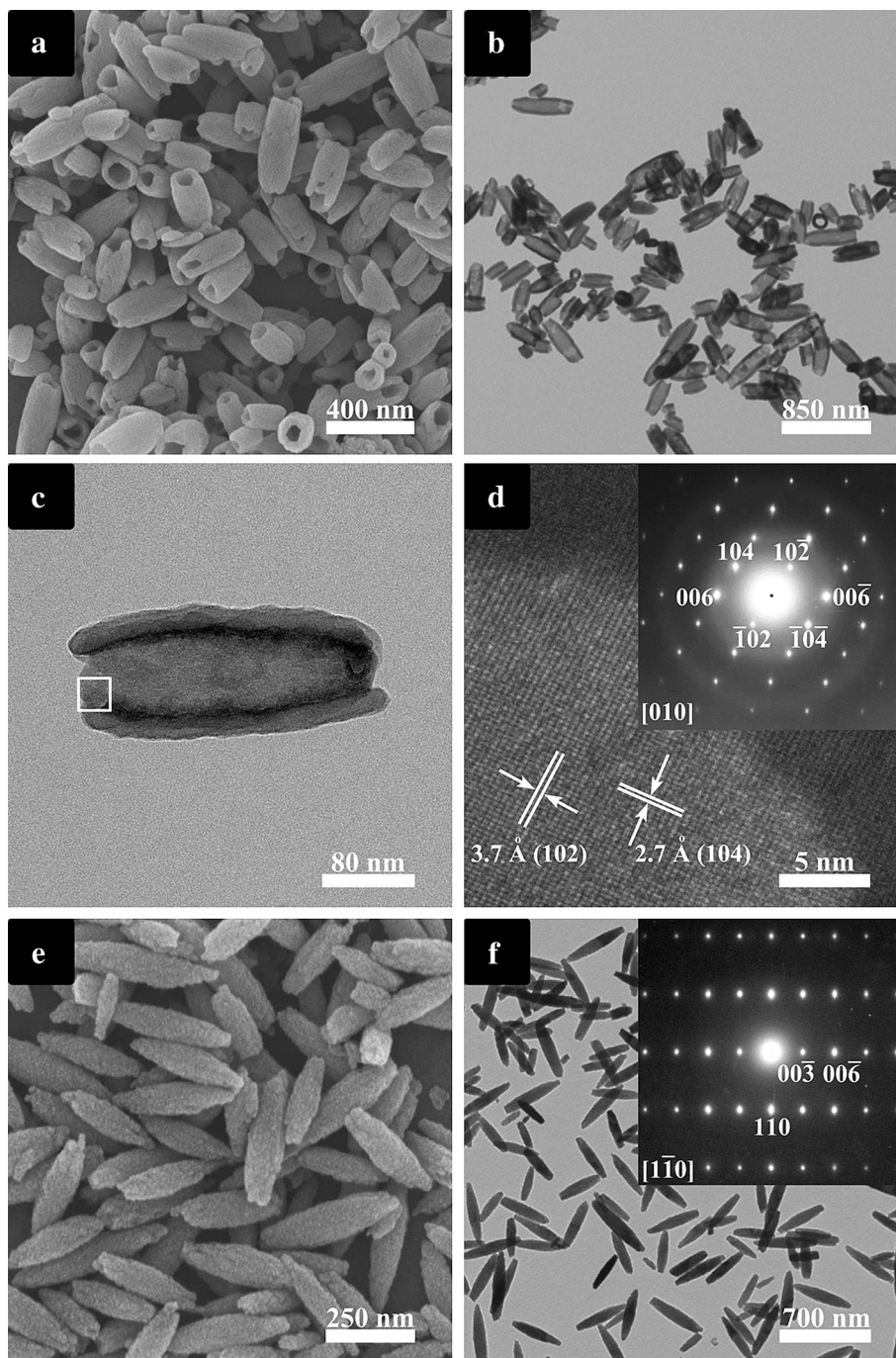


Fig. 1. XRD patterns of the FNTs and FNRs.



**Fig. 2.** SEM image (a), TEM image at a low magnification (b) and a high magnification (c), and HRTEM image (d) (inset: SAED pattern) of FNTs. SEM image (e), and TEM image (f) (inset: SAED pattern) of FNRs.

result from the XRD pattern. The SAED pattern further verifies the single-crystalline feature of the FNTs. As described in Fig. 2e and f, the FNRs are presented as the spindle-like nanorods with a length of 200–400 nm and a diameter of about 50–70 nm, close to the sizes of the FNTs. The SAED patterns of the FNRs (the inset of Fig. 2f) suggest the growth direction of the FNRs is along  $\langle 001 \rangle$ , consistent with that of the FNTs.

### 3.2. Electrochemical characterization

Galvanostatic discharge/charge tests were carried out within a voltage window of 0.05–3.0 V at a current density of  $100 \text{ mA g}^{-1}$

for both electrodes. As shown in Fig. 3a, the first discharge plateau of the FNTs appears at 1.5 V, which has been reported as a feature for lithium insertion in  $\alpha\text{-Fe}_2\text{O}_3$  to form  $\alpha\text{-LiFe}_2\text{O}_3$  [29,30]. Then, the plateau is followed by a smooth voltage drop to 0.87 V, which could be attributed to the transformation from rhombohedral  $\alpha\text{-LiFe}_2\text{O}_3$  to cubic  $\text{Li}_x\text{Fe}_2\text{O}_3$  [29,30]. After that, the complete conversion from  $\text{Li}_x\text{Fe}_2\text{O}_3$  to metal  $\text{Fe}^0$  produces the second plateau at 0.87 V. Finally, the voltage gradually decreases to 0.05 V. The total discharge capacity of the first cycle is  $1384 \text{ mAh g}^{-1}$  for the FNTs, about 8 mol of Li per formula unit. The excess capacity probably comes from the formation of a solid electrolyte interphase (SEI) on the surface [10,31]. When the electrode is charged to 3.0 V, a pronounced



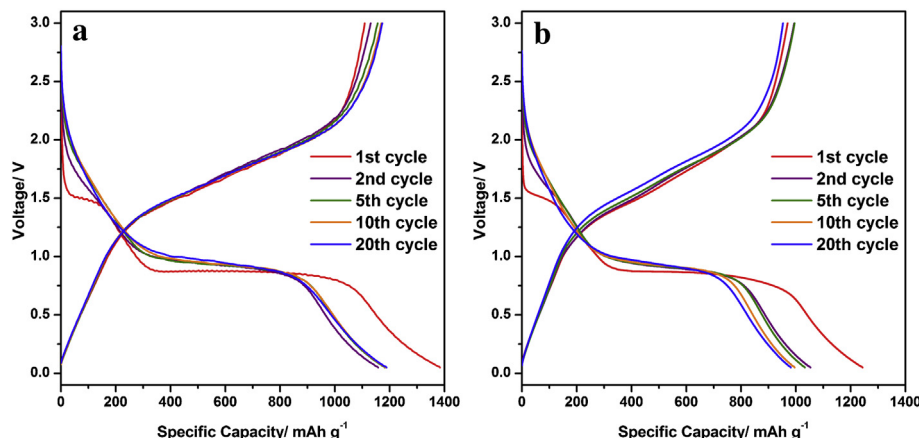


Fig. 3. Discharge–charge voltage profiles of the electrodes made of (a) FNTs and (b) FNRs. Both electrodes are cycled at  $100 \text{ mA g}^{-1}$ .

voltage plateau is observed between 1.3 V and 2.3 V, corresponding to a charge capacity of  $1108 \text{ mAh g}^{-1}$ . Started from the second cycle, the discharge/charge profiles become similar to each other, indicating the highly reversibility of the lithiation/delithiation processes. The coulombic efficiency of the FNTs increases to 97% from the second cycle. The similar case also happens to the electrodes made by the FNRs, as presented in Fig. 3b. But the initial discharge and charge capacities of the FNRs are 1243 and  $970 \text{ mAh g}^{-1}$ , respectively.

Fig. 4a shows the reversible capacities of the electrodes made by FNTs and FNRs at a current density of  $100 \text{ mA g}^{-1}$ . Compared with the FNRs with a solid interior, the FNTs with a tubular morphology exhibit the higher reversible capacity as well as the better capacity retention. After 60 cycles, the electrodes made by the FNTs and the FNRs deliver the reversible capacities of about 1200 and  $920 \text{ mAh g}^{-1}$ , respectively. The slight increase of the reversible capacity of the FNTs after the first cycle, might originate from the effect of the CMC binder [23,32] and the rearrangement of the structures of FNTs during cycling [33]. The cycling performances of the FNTs and the FNRs at a large current density are also measured at  $500 \text{ mA g}^{-1}$  (Fig. 4b). Compared with the results at  $100 \text{ mA g}^{-1}$ , there are significant decreases for the reversible capacities of both electrodes at  $500 \text{ mA g}^{-1}$ . The reversible capacity of the FNRs goes down to  $360 \text{ mAh g}^{-1}$  after 60 cycles. However, the FNTs retain a good reversible capacity of  $1030 \text{ mAh g}^{-1}$  after 60 cycles, nearly three times the theoretical capacity of graphite. This difference in

reversible capacity indicates the advantage of the FNTs in the lithium-storage performance over the FNRs.

Since the FNTs and the FNRs have the same chemical component and close size, the superior performance of the FNTs is likely to be related with their unique structure. In order to get more insights at this point, the electrodes after 60 cycles at a current density of  $500 \text{ mA g}^{-1}$  are checked by TEM images. As presented in Fig. 5a and Fig. 5b, the FNTs still preserve their tubular morphology, although they exhibit the deformation to some extent. This result could be attributed to the hollow space of the FNTs that provides enough rooms for the volume change during lithiation/delithiation processes. The nanoparticles distributed around the nanotubes are probably carbon black used in the fabrication of the electrodes. The FNRs have been pulverized to many aggregated nanoparticles, as observed in Fig. 5c and d. This result would lead to a poor electrical contact between the neighboring nanoparticles and a decrease of electric conductivity.

The increased electric conductivity of the FNTs has been supported by electro-chemical impedance spectra (EIS) (Fig. 6a) and current interruption technique (Fig. 6b). The EIS spectra of the electrodes made by FNTs and FNRs could be well fitted by the Nyquist plots that consist of a semicircle in the high-to-medium frequency region and a slope line in the low frequency region. The intercept of the plots at the real axis corresponds to the ohmic resistance ( $R_0$ ). As the same electrolyte and the identical cell configurations are employed, both of the electrodes should have

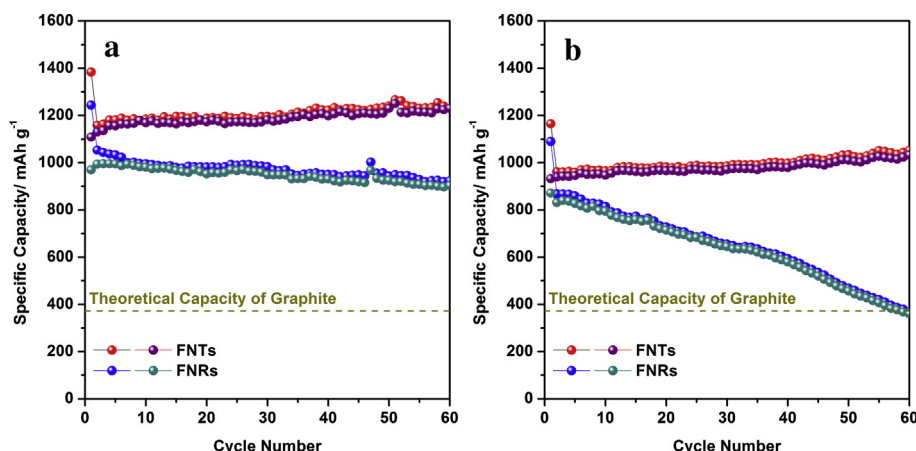


Fig. 4. Cycling performances of the electrodes made of FNTs and FNRs cycled at  $100 \text{ mA g}^{-1}$  (a) and  $500 \text{ mA g}^{-1}$  (b).

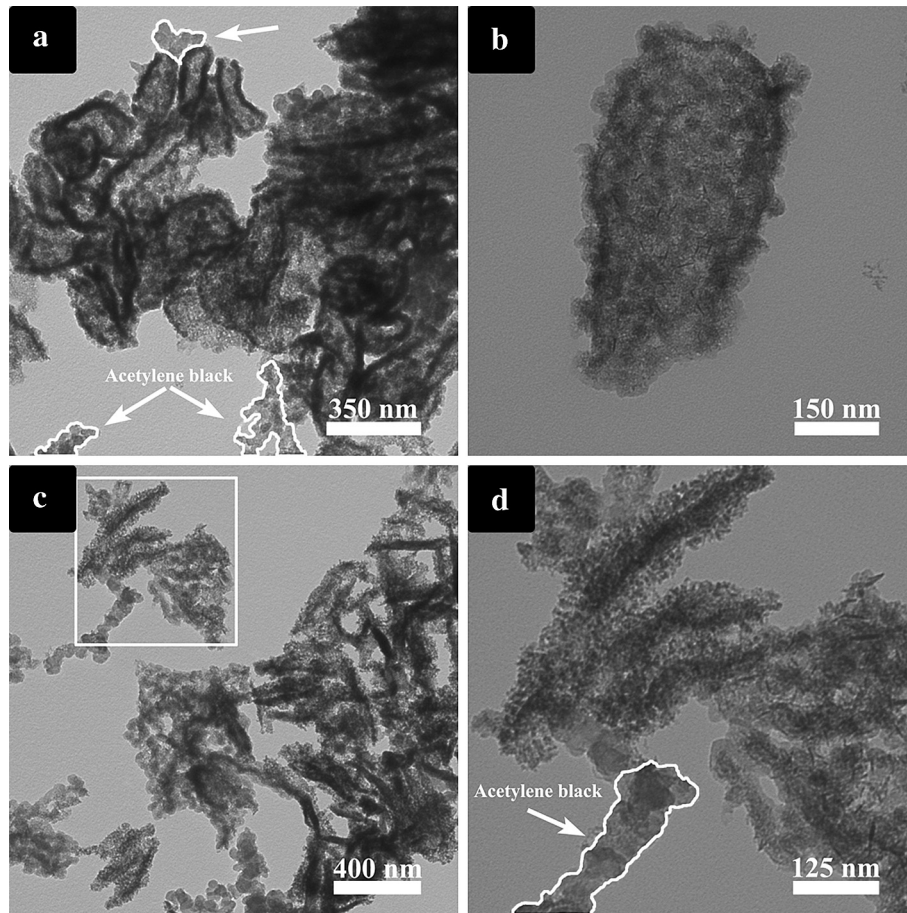


Fig. 5. TEM images of the electrodes made of FNTs (a, b) and FNRs (c, d) after 60 cycles at  $500 \text{ mA g}^{-1}$ .

similar value of  $R_{\Omega}$ . The semicircle in the high-to-medium frequency region is related to the interfacial charge-transfer resistance ( $R_{ct}$ ) and the oblique line followed with the semicircle represents the Warburg impedance ( $Z_w$ ). [21] As shown in Fig. 6a, it can be concluded that the charge-transfer resistance of the FNTs is smaller than that of the FNRs. This result suggests that the electron transfer is easier in the electrode made of FNTs, benefiting the enhancement of its lithium-storage performance. The plots of the DC versus SOC for the FNTs and the FNRs are shown in Fig. 6b. The DC resistances

of the two electrodes undergo small changes and show similar values before 55% SOC. After that, the DC resistance of the FNRs increases more rapidly than that of the FNTs electrode. This result indicates that the presence of the tubular structure could effectively reduce the DC resistance of hematite electrode, facilitating the electron transportation.

Beside the good structure stability and high electrical conductivity, the FNTs also have a large specific surface area, which would increase the contact between the electrode and the electrolyte and

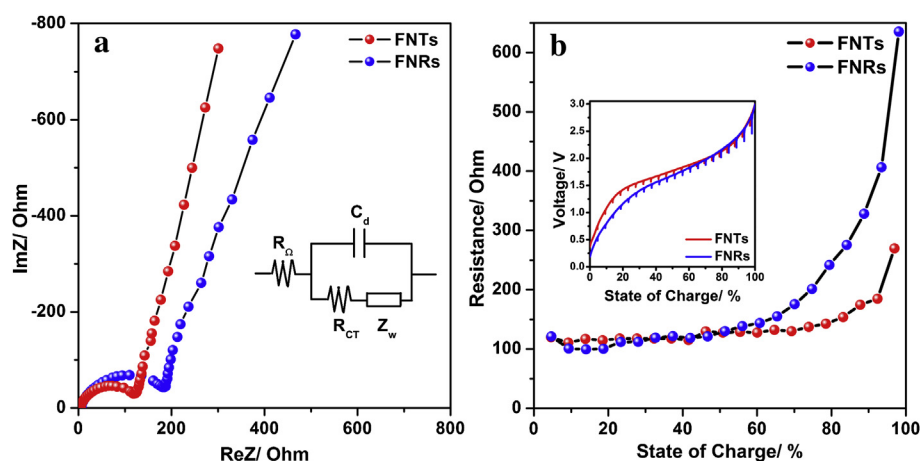


Fig. 6. (a) Electrochemical impedance spectra of electrodes made of FNTs and FNRs at open-circuit voltage; (b) plots of the direct current resistances of the electrodes made of FNTs and FNRs vs. state of charge. The inset is the charge profiles of electrodes made of FNTs and FNRs measured by the current interruption technique, after 50 cycles at  $500 \text{ mA g}^{-1}$ .

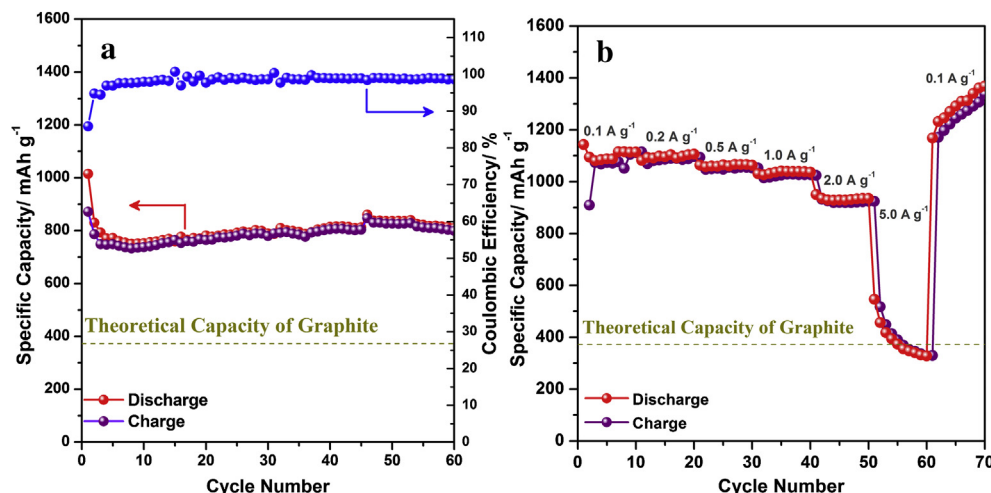


Fig. 7. (a) Cycling performance of the electrodes made of FNTs cycled at 1000 mA g<sup>-1</sup>; (b) rate performance of the electrodes made of FNTs.

then facilitate the lithiation/delithiation processes of the electrode [34,35]. The large specific surface area of the nanotubes is confirmed by N<sub>2</sub> absorption–desorption isotherm. The specific surface areas of the FNTs and the FNRs calculated by the Brunauer–Emmett–Teller (BET) method, are 38.4 and 13.5 m<sup>2</sup> g<sup>-1</sup>, respectively.

To further investigate the lithium-storage performance of the FNTs electrode at a high rate, the electrodes made of the FNTs are cycled at 1000 mA g<sup>-1</sup> (Fig. 7a). The initial discharge and charge capacities of FNTs electrode are 1015 and 872 mAh g<sup>-1</sup> respectively. During the following cycles, the discharge capacity could be retained at 810 mAh g<sup>-1</sup> after 60 cycles, with a coulombic efficiency of 98%. This result implies the good cycling stability of the FNTs. The rate performance of the FNTs is tested from 100 to 5000 mA g<sup>-1</sup> (100, 200, 500, 1000, 2000 and 5000 mA g<sup>-1</sup>) with each current density for 10 cycles (Fig. 7b). When cycled at a high current density of 2000 mA g<sup>-1</sup>, the FNTs present a reversible capacity of 930 mAh g<sup>-1</sup> for 10 cycles, which is more than twice the theoretical limit of graphite. As the current density rises to 5000 mA g<sup>-1</sup>, the capacity retention becomes worse and only holds a capacity of 330 mAh g<sup>-1</sup> after 10 cycles. Such a sudden drop might originate from the collapse of the tubular structure.

#### 4. Conclusion

Single-crystalline hematite nanotubes and nanorods with the similar sizes were successfully prepared via a hydrothermal method without further thermal annealing process. It is found that the electrodes made by  $\alpha$ -Fe<sub>2</sub>O<sub>3</sub> nanotubes could exhibit a reversible capacity of 1200 mAh g<sup>-1</sup> at 100 mA g<sup>-1</sup>, 1000 mAh g<sup>-1</sup> at 500 mA g<sup>-1</sup>, and 810 mAh g<sup>-1</sup> at 1000 mA g<sup>-1</sup> after 60 cycles, much better than those of the electrode made by the nanorods. The improved lithium storage performance of the nanotubes can be attributed to the unique tubular structure, which offers enough room for the volume variation during lithiation/delithiation processes and shortens the pathways of the lithium transportation. So, the nanotubes could keep the structure integrity and exhibit the superior electric conductivity to the nanorods.

#### Acknowledgments

This work was supported by the 973 Project of China (2011CB935901), Natural Science Foundation of China (91022033,

21071055, 51172076, 21203111), New Century Excellent Talents in University (NCET-10-0369), Shandong Provincial Natural Science Foundation for Distinguished Young Scholar (JQ201205), Independent Innovation Foundations of Shandong University (2012 ZD007), and New Faculty start-up funding in Shandong University.

#### References

- [1] P. Poizot, S. Laruelle, S. Grugeon, L. Dupont, J.M. Tarascon, *Nature* 407 (2000) 496–499.
- [2] A. Ponrouch, P.L. Taberna, P. Simon, M.R. Palacín, *Electrochim. Acta* 61 (2012) 13–18.
- [3] L. Zou, F. Kang, X. Li, Y.P. Zheng, W. Shen, J. Zhang, *J. Phys. Chem. Solids* 69 (2008) 1265–1271.
- [4] A.S. Arico, P. Bruce, B. Scrosati, J.M. Tarascon, W. van Schalkwijk, *Nat. Mater.* 4 (2005) 366–377.
- [5] X.L. Wu, Y.G. Guo, L.J. Wan, C.W. Hu, *J. Phys. Chem. C* 112 (2008) 16824–16829.
- [6] P. Zhang, Z.P. Guo, H.K. Liu, *Electrochim. Acta* 55 (2010) 8521–8526.
- [7] X.C. Duan, L. Mei, J.M. Ma, Q.H. Li, T.H. Wang, W.J. Zheng, *Chem. Commun.* 48 (2012) 12204–12206.
- [8] M.S. Wu, Y.H. Ou, Y.P. Lin, *J. Electrochem. Soc.* 158 (2011) A231–A236.
- [9] B. Jang, M. Park, O.B. Chae, S. Park, Y. Kim, S.M. Oh, Y. Piao, T. Hyeon, *J. Am. Chem. Soc.* 134 (2012) 15010–15015.
- [10] M.V. Reddy, T. Yu, C.H. Sow, Z.X. Shen, C.T. Lim, G.V. Subba Rao, B.V.R. Chowdari, *Adv. Funct. Mater.* 17 (2007) 2792–2799.
- [11] L. Chun, X. Wu, X. Lou, Y. Zhang, *Electrochim. Acta* 55 (2010) 3089–3092.
- [12] D.N. Lei, M. Zhang, B.H. Qu, L.B. Chen, Y.G. Wang, E.D. Zhang, Z. Xu, Q.H. Li, T.H. Wang, *Nanoscale* 4 (2012) 3422–3426.
- [13] J. Lu, Q. Peng, Z.Y. Wang, C.Y. Nan, L.H. Li, Y.D. Li, *J. Mater. Chem. A* 1 (2013) 5232–5237.
- [14] S. Zeng, K. Tang, T. Li, Z. Liang, D. Wang, Y. Wang, Y. Qi, W. Zhou, *J. Phys. Chem. C* 112 (2008) 4836–4843.
- [15] Y. Han, Y. Wang, L. Li, Y. Wang, L. Jiao, H. Yuan, S. Liu, *Electrochim. Acta* 56 (2011) 3175–3181.
- [16] X.H. Ma, X.Y. Feng, C. Song, B.K. Zou, C.X. Ding, Y. Yu, C.H. Chen, *Electrochim. Acta* 93 (2013) 131–136.
- [17] J. Chen, L. Xu, W. Li, X. Gou, *Adv. Mater.* 17 (2005) 582–586.
- [18] J. Liu, Y. Li, H. Fan, Z. Zhu, J. Jiang, R. Ding, Y. Hu, X. Huang, *Chem. Mater.* 22 (2010) 212–217.
- [19] Z. Wang, D. Luan, S. Madhavi, C.M. Li, X.W. Lou, *Chem. Commun.* 47 (2011) 8061–8063.
- [20] C. Wu, P. Yin, X. Zhu, C. OuYang, Y. Xie, *J. Phys. Chem. B* 110 (2006) 17806–17812.
- [21] H. Liu, G. Wang, J. Park, J. Wang, H. Liu, C. Zhang, *Electrochim. Acta* 54 (2009) 1733–1736.
- [22] Y. Song, S. Qin, Y. Zhang, W. Gao, J. Liu, *J. Phys. Chem. C* 114 (2010) 21158–21164.
- [23] Y.M. Lin, P.R. Abel, A. Heller, C.B. Mullins, *J. Phys. Chem. Lett.* 2 (2011) 2885–2891.
- [24] C.T. Cheria, J. Sundaramurthy, M. Kalaivani, P. Ragupathy, P.S. Kumar, V. Thavasi, M.V. Reddy, C.H. Sow, S.G. Mhaisalkar, S. Ramakrishna, B.V.R. Chowdari, *J. Mater. Chem.* 22 (2012) 12198–12204.
- [25] G. Centi, S. Perathoner, *Eur. J. Inorg. Chem.* 2009 (2009) 3851–3878.
- [26] Y. Nuli, R. Zeng, P. Zhang, Z. Guo, H. Liu, *J. Power Sources* 184 (2008) 456–461.

- [27] C.J. Jia, L.D. Sun, Z.G. Yan, L.P. You, F. Luo, X.D. Han, Y.C. Pang, Z. Zhang, C.H. Yan, *Angew. Chem. Int. Ed.* 44 (2005) 4328–4333.
- [28] H.Y. Xu, S. Xie, N. Ding, B.L. Liu, Y. Shang, C.H. Chen, *Electrochim. Acta* 51 (2006) 4352–4357.
- [29] D. Larcher, C. Masquelier, D. Bonnin, Y. Chabre, V. Masson, J.B. Leriche, J.M. Tarascon, *J. Electrochem. Soc.* 150 (2003) A133–A139.
- [30] D. Larcher, D. Bonnin, R. Cortes, I. Rivals, L. Personnaz, J.M. Tarascon, *J. Electrochem. Soc.* 150 (2003) A1643–A1650.
- [31] P. Tartaj, J.M. Amarilla, J. Power Sources 196 (2011) 2164–2170.
- [32] J. Li, H.M. Dahn, L.J. Krause, D.B. Le, J.R. Dahn, *J. Electrochem. Soc.* 155 (2008) A812–A816.
- [33] J. Zhang, Y. Sun, Y. Yao, T. Huang, A. Yu, *J. Power Sources* 222 (2013) 59–65.
- [34] M.H. Park, M.G. Kim, J. Joo, K. Kim, J. Kim, S. Ahn, Y. Cui, J. Cho, *Nano Lett.* 9 (2009) 3844–3847.
- [35] J.K. Yoo, J. Kim, Y.S. Jung, K. Kang, *Adv. Mater.* 24 (2012) 5452–5456.